



# Improving BDS-3 precise orbit determination for medium earth orbit satellites

Xingxing Li<sup>1</sup> · Yongqiang Yuan<sup>1</sup> · Yiting Zhu<sup>1</sup> · Wenhai Jiao<sup>2</sup> · Lang Bian<sup>3</sup> · Xin Li<sup>1</sup> · Keke Zhang<sup>1</sup>

Received: 28 September 2019 / Accepted: 26 February 2020 / Published online: 6 March 2020  
© Springer-Verlag GmbH Germany, part of Springer Nature 2020

## Abstract

As of June 2019, 18 BDS-3 medium earth orbit (MEO) satellites have been launched into orbit. We perform precise orbit determination for these BDS-3 satellites with the rate-limited attitude models and the a priori box-wing solar radiation pressure model. The BDS-3 MEO satellites employ continuous yaw-steering attitude mode. By using proper yaw-attitude models during deep eclipse seasons, the orbit overlapping can be reduced by (0.6, 0.5, 0.4) cm for satellites developed by China Academy of Space Technology (CAST) and (0.5, 0.4, 0.3) cm for satellites developed by Shanghai Engineering Center for Microsatellites (SECM) in along-track, cross-track, and radial components, respectively. Compared to nominal attitudes, the attitude models also reduce the RMS of ionospheric-free carrier-phase residuals from 1.87 cm and 1.83 cm to 1.74 cm and 1.79 cm for CAST and SECM satellites in deep eclipse seasons, respectively. In addition, the satellite clock residuals become smoother by using the rate-limited yaw-attitude models. By applying the a priori box-wing SRP model along with a 5-parameter extended CODE orbit model (ECOM1), the orbit overlapping can be reduced to (6.9, 3.8, 1.9) cm for CAST satellites and (10.6, 5.8, 2.4) cm for SECM satellites, which are (0.6, 0.7, 0.6) cm and (0.7, 0.5, 0.7) cm smaller compared to those of the updated ECOM model (ECOM2). The BDS-3 orbits are then validated by satellite laser ranging (SLR), and the results demonstrate mean biases of 0–5 cm with standard derivations of 3–6 cm. The SLR validation also reveals that using an a priori box-wing model can reduce the SLR mean biases and standard deviations when compared to the ECOM2 model.

**Keywords** BDS-3 · Precise orbit determination (POD) · Yaw-attitude · Solar radiation pressure (SRP)

## Introduction

The construction of Chinese BeiDou navigation satellite system can be divided into three phases, that is, the BeiDou Navigation Satellite Demonstration System (BDS-1), the regional BeiDou Navigation Satellite System (BDS-2), and the BeiDou Navigation Satellite System with global coverage (BDS-3) (Yang et al. 2011). BDS-1 was accomplished in 2003 (Yang et al. 2017), and BDS-2 has been providing operational navigation services for China and the Asia-Pacific region since the end of 2012. Initial results of

precise orbit determination (POD) for BDS-2 were presented by Shi et al. (2012), He et al. (2013), Steigenberger et al. (2013), and Li et al. (2015).

In 2015, China started the expansion of BDS from regional to worldwide coverage, and the first new-generation BDS satellite (BDS-3 experimental, denoted as “BDS-3S”) was launched on March 30, 2015. By February 2016, a total of five BDS-3S satellites have been brought into orbit, including two inclined geosynchronous orbit (IGSO) and three medium earth orbit (MEO) satellites. Different from BDS-2, BDS-3S satellites transmit signals on five frequencies of B1I, B3I, B1C, B2a, and B2b (Xiao et al. 2016; CSNO 2017a, b). Initial assessments of BDS-3S navigation signals were presented by Zhang et al. (2017a, b). The results revealed that the satellite-induced code bias (Wanninger and Beer 2015) almost vanishes for BDS-3S signals, and the observation quality of BDS-3S is comparable to that of GPS and Galileo. Tan et al. (2016) reported the initial POD results of BDS-3S satellites based on 9 stations from the international GNSS Monitoring and Assessment System

✉ Xingxing Li  
lxlq109121@gmail.com

<sup>1</sup> School of Geodesy and Geomatics, Wuhan University, 129 Luoyu Road, Wuhan 430079, Hubei, China

<sup>2</sup> China Beijing Institute of Tracking and Telecommunication Technology, Beijing 100094, China

<sup>3</sup> China Academy of Space Technology (Xi'an), Xi'an, China

(iGMAS; Jiao et al. 2011). Li et al. (2018a) demonstrated that no obvious systematic bias exists between BDS-3S and BDS-2 in their common B1I and B3I signals and that BDS-3S IGSO-1S most likely still uses an orbit-normal (ON) mode. Zhao et al. (2017) estimated the yaw-attitude of BDS-3S MEO-1S, MEO-2S, and IGSO-2S based on the reverse kinematic precise point positioning approach, and the results indicated that these satellites employ continuous yaw-steering (YS) mode with midnight and noon maneuvers. In addition, Wang et al. (2018) applied an a priori solar radiation pressure (SRP) model together with the extended CODE orbit model (ECOM1; Springer et al. 1999) to reduce orbit modeling deficiency for BDS-3S IGSO-2S. An orbit accuracy improvement of 35% in the radial component can be observed when using the a priori SRP model.

The buildup of the BDS-3 constellation was initiated on November 5, 2017. As of June 2019, a total of 21 satellites have been sent into orbit through 12 launches, including 18 MEO, 1 geostationary earth orbit (GEO), and 2 IGSO satellites. BDS-3 satellites transmit five open service signals of B1I, B3I, B1C, B2a, and B2b. The modulation techniques and the detailed signal structures of B1C and B2a are introduced in Lu et al. (2019). Using stations of iGMAS network, Yan et al. (2018) analyzed the quality of BDS-3 signals, and the results showed that B1C has a lower carrier-to-noise-density ratio than B1I, B3I, and B2a, and the pseudorange code of B1C is noisier than that of B1I, B3I and B2a. Zhang et al. (2019) reported that the signal intensity of BDS-3 B1I and B3I is better than that of BDS-2. Xu et al. (2019) compared the POD performances of two ionospheric-free combinations, e.g., the combination of B1I+B3I and the combination of B1C+B2a. The results demonstrated a better POD performance of the B1I+B3I combination in terms of the 48-h overlapping RMS values, which are 1.3, 0.7, and 0.1 cm smaller than those of B1C+B2a combination in the along-track, cross-track and radial components, respectively. Using the B1I+B3I observations from about 100 stations in both iGMAS and the International GNSS Service (IGS; Johnston et al. 2017) networks, Xu et al. (2019) achieved the satellite laser ranging (SLR) validation accuracy of about 4–6 cm for BDS-3 satellites. In addition, Yan et al. (2019) presented an a priori cuboid SRP model for BDS-3 MEO satellites based on the adjustable box-wing model (Rodriguez-Solano et al. 2012). Compared to the empirical ECOM1 and ECOM2 (Arnold et al. 2015) models, the a priori cuboid SRP model can reduce the systematic variation of the SLR residuals.

We focus on POD for the BDS-3 MEO satellites. Several critical issues in orbit modeling, including attitude models and the BDS-3 a priori box-wing SRP models, will be studied to improve BDS-3 POD performance further. The current BDS-3 constellation and BDS-3 tracking networks are characterized first. Then, the POD processing strategies are

summarized. In the following, the influences of BDS-3 yaw-attitude models on POD and the BDS-3 a priori box-wing SRP model are demonstrated. Finally, the conclusions and discussions are provided.

## BDS-3 constellation and tracking networks

Since 2017, a total of 18 BDS-3 MEO satellites have been launched into orbit. In this section, the basic status of current BDS-3 constellation is first introduced. Then the ground tracking networks of BDS-3 satellites are described, including the iGMAS network and the Multi-GNSS Experiment (MGEX; Montenbruck et al. 2017b) network.

### Current BDS-3 constellation

The construction of the BDS-3 constellation was initiated on November 5, 2017, with successful launches of a pair of BDS-3 MEO satellites. In 2018, China entered a period with an unprecedentedly high launching rate of BeiDou satellites. Eight pairs of BDS-3 satellites were sent to orbit on January 11, February 12, March 29, July 29, August 24, September 19, October 15, and November 18 in 2018, respectively. BDS-3 MEO satellites employ two different satellite platforms developed by China Academy of Space Technology (CAST) and Shanghai Engineering Center for Microsatellites (SECM), with different satellite body sizes and different attitude modes. Each CAST satellite is equipped with two Rubidium Atomic Frequency Standards (RAFSs) made from China Aerospace Science and Technology Corporation (CASC) and two RAFSs from China Aerospace Science and Industry Corporation (CASIC), while each SECM satellite carries two Passive Hydrogen Masers (PHMs) from Shanghai Astronomical Observatory (SHAO) and two RAFSs from CASIC ([http://mgex.igs.org/IGS\\_MGEX\\_Status\\_BDS.php](http://mgex.igs.org/IGS_MGEX_Status_BDS.php)). At the end of 2018, BDS-3 started to provide global services. The BDS-3 constellation with 30 satellites is planned to be completed by about 2020. The status of the BDS-3 constellations is summarized in Table 1.

### BDS-3 tracking networks

By June 2019, the iGMAS network (Jiao et al. 2011) consists of 24 stations, among which 23 stations equipped with GNSS\_GGR, CETC-54-GMR-4011, and CETC-54-GMR-4016 receivers of China Electronics Technology Group Corporation and UNICORE UB4B01 receivers of Unicore Communications can track BDS-3 B1I, B3I, B1C, and B2a signals (listed in Table 2). Their distribution is demonstrated as red pentagrams in Fig. 1.

Initiated by IGS, the MGEX project aims to build up a global network, collect and characterize new signals, and

**Table 1** Status of BDS-3 (as of June 2019; [http://mgex.igs.org/IGS\\_MGEX\\_Status\\_BDS.php](http://mgex.igs.org/IGS_MGEX_Status_BDS.php))

Space vehicle number (SVN)	Common name	Pseudo-random noise (PRN) number	Launch date; notes
C201	BeiDou-3 MEO-1	C19/C47	2017/11/05; CAST; PRN C19 used until 2018/06/12 and since 2018/11/15
C202	BeiDou-3 MEO-2	C20	2017/11/05; CAST
C203	BeiDou-3 MEO-7	C27	2018/01/11; SECM
C204	BeiDou-3 MEO-8	C28/C48	2018/01/11; SECM; PRN C28 used until 2018/06/11 and since 2018/12/20
C205	BeiDou-3 MEO-4	C22	2018/02/12; CAST
C206	BeiDou-3 MEO-3	C21	2018/02/12; CAST
C207	BeiDou-3 MEO-9	C29	2018/03/29; SECM
C208	BeiDou-3 MEO-10	C30	2018/03/29; SECM
C209	BeiDou-3 MEO-5	C23	2018/07/29; CAST
C210	BeiDou-3 MEO-6	C24	2018/07/29; CAST
C211	BeiDou-3 MEO-12	C26	2018/08/24; SECM
C212	BeiDou-3 MEO-11	C25	2018/08/24; SECM
C213	BeiDou-3 MEO-13	C32	2018/09/19; CAST
C214	BeiDou-3 MEO-14	C33	2018/09/19; CAST
C215	BeiDou-3 MEO-16	C35	2018/10/15; SECM
C216	BeiDou-3 MEO-15	C34	2018/10/15; SECM
C217	BeiDou-3 GEO-1	C59	2018/11/01; CAST
C218	BeiDou-3 MEO-17	C36	2018/11/18; CAST
C219	BeiDou-3 MEO-18	C37	2018/11/18; CAST
C220	BeiDou-3 IGSO-1	C38	2019/04/20; CAST
C221	BeiDou-3 IGSO-2	C39	2019/06/24; CAST

generate products for the emerging GNSS including BDS. By June 2019, the MGEX network has grown to more than 300 stations, among which 75 stations are capable of tracking BDS-3 B1I and B3I signals. These MGEX BDS-3 tracking stations (blue triangles in Fig. 1) are equipped with JAVAD TRE\_3 DELTA, TRIMBLE NETR9/ALLOY, and SEPT POLARX5/POLARX5TR receivers. Both the MGEX and iGMAS stations are selected for BDS-3 POD. However, neither TRIMBLE NETR9/ALLOY nor SEPT POLARX5/POLARX5TR receivers can provide observations of C215, C218, and C219 (with PRNs of C35, C36, and C37) during the study period (DOY 001–130, 2019). Therefore, we focus on the precise orbit determination for the other 15 BDS-3 MEO satellites in this contribution.

## BDS-3 POD strategies

Datasets of 130 days during DOY 001–130, 2019 are processed to investigate two critical issues in BDS-3 POD: BDS-3 POD with rate-limited attitude models, and BDS-3 POD with the a priori box-wing SRP model. POD results

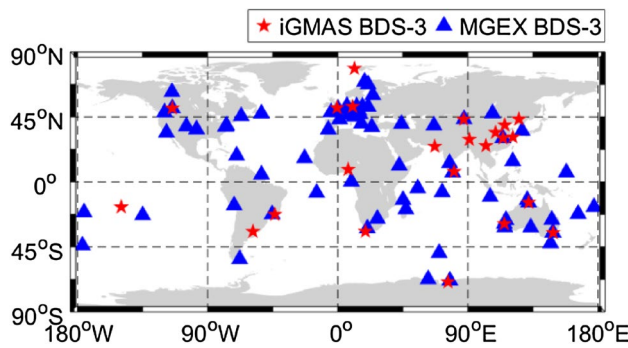
are evaluated by orbit overlapping comparisons as well as SLR validations. For any two adjacent 3-day orbit solutions shifted by 2 days, there is a common day that can be treated as the overlapping arc. In this study, the 24-h orbit overlapping is used to validate the POD results.

The block-specific phase center offset (PCO) values of BDS-3 satellites for three frequency bands of B1, B2, and B3 are summarized in Table 3. These values are provided by the Test and Assessment Research Center of China Satellite Navigation Office (CSNO/TARC) and have been added to the absolute IGS antenna correction file in June 2019 (Villiger 2019). Please note that the PCOs in Table 3 differ from those released by CSNO (2019a) by several centimeters. Slightly differences would be observed in the POD results when using different PCO values. Due to the lack of receiver antenna calibrations for BDS signals, the GPS L1/L2 PCOs and phase center variations (PCVs) are also applied for BDS-3 B1I/B3I, respectively. Ionospheric-free code (PC) and carrier-phase (LC) combinations are used to eliminate the first-order ionospheric delays.

The earth tide, ocean tide loading, phase wind-up can be corrected according to the existing models (Petit and Luzum

**Table 2** iGMAS BDS-3 tracking stations

Stations	Location	Country	Receiver code	Antenna code
ABJA	Abuja	Nigeria	GNSS_GGR	RINT-8CH CETD
BJF1	Beijing	China	CETC-54-GMR-4016	LEIAR25.R4 LEIT
BRCH	Braunschweig	Germany	CETC-54-GMR-4016	NOV750.R4 NOVS
BYNS	Buenos Aires	Argentina	UNICORE UB4B0I	NOV750.R4 NOVS
CANB	Canberra	Australia	CETC-54-GMR-4011	GNSS-750
CHU1	Changchun	China	GNSS_GGR	RINT-8CH CETD
CLGY	Calgary	Canada	CETC-54-GMR-4016	LEIAR25.R4 LEIT
CNYR	Huanghe Station	Arctic	UNICORE UB4B0I	NOV750.R4 NOVS
DWIN	Darwin	Australia	CETC-54-GMR-4011	GNSS-750
GUA1	Urumqi	China	GNSS_GGR	RINT-8CH CETD
HMNS	Hermanus	South Africa	GNSS_GGR	RINT-8CH CETD
ICUK	London	United Kingdom	CETC-54-GMR-4016	NovAtel-750
KNDY	Kandy	Sri Lanka	CETC-54-GMR-4016	GNSS-750
KUN1	Kunming	China	UNICORE UB4B0I	NOV750.R4 NOVS
KRCH	Karachi	Pakistan	UNICORE UB4B0I	NOV750.R4 NOVS
LHA1	Lhasa	China	CETC-54-GMR-4016	NOV750.R4 NOVS
PETH	Perth	Australia	CETC-54-GMR-4011	GNSS-750
RDJN	Rio de Janeiro	Brazil	UNICORE UB4B0I	NOV750.R4 NOVS
SHA1	Shanghai	China	UNICORE UB4B0I	NOV750.R4 NOVS
TAHT	Tahiti	France	GNSS_GGR	RINT-8CH CETD
WUH1	Wuhan	China	CETC-54-GMR-4016	LEIAR25.R4 LEIT
XIA1	Xi'an	China	GNSS_GGR	RINT-8CH CETD
ZHON	Zhongshan Station	Antarctica	CETC-54-GMR-4011	GNSS-750

**Fig. 1** Distribution of tracking stations selected for BDS-3 POD. Red pentagrams are iGMAS stations, and blue triangles are MGEX stations

while the coordinates of iGMAS stations are estimated in POD. The joint processing with GPS will improve the performance of BDS-3 POD since more satellites will result in a superior estimation of common parameters such as station coordinates, tropospheric parameters and receiver clock offsets. Double-differenced (DD) ambiguity resolution (AR) is applied for GPS and BDS-3 separately. No DD AR is implemented for ambiguities from different systems. Table 4 summarizes the detailed information of the POD strategies including observation models, dynamical models, and estimated parameters.

## POD performance of BDS-3

In this section, the attitude control models are described for CAST and SECM satellites, respectively. The POD performances with the nominal yaw-steering attitude without rate limitations and the block-specific yaw-attitude models with rate limitations are compared in terms of observation residuals, orbit overlapping comparison, and clock residuals. Furthermore, the approximate satellite dimensions and optical properties are introduced, with the help of which the BDS-3 a priori box-wing SRP model can be established and assessed.

2010; Lyard et al. 2006; Wu et al. 1993). The coordinates of MGEX stations are fixed to IGS weekly combined solution,

**Table 4** Processing strategies of BDS-3 POD

Items	Models
Observations	BDS-3: B1I and B3I; GPS: C1C/L1C for L1 band; C2L/L2L and C2W/L2W for L2 band; differential code biases are corrected by the products provided by DLR (Montenbruck et al. 2014) Standard deviation of observations: 2 m for each raw code observation and 2 mm for each raw carrier-phase observation
POD arc	3 days arc length, 300 s sampling
Observation weight	Elevation dependent with 7 deg cutoff. 1 for $E > 30$ deg, otherwise $2 * \sin(E)$
Geopotential	12 × 12 EGM2008 model (Pavlis et al. 2012)
N-body	Jet Propulsion Laboratory (JPL) DE405 (Standish 1998)
Attitude mode	Continuous yaw-steering for BDS-3 For GPS: attitude models by Kouba (2008) are adopted for Block IIA/IIR satellites; the models by Dilssner (2010a) and Kouba (2013) are adopted for Block IIF satellites
Solar radiation	The updated ECOM model (ECOM2) with 9 parameters of D4B1 (Arnold et al. 2015) and the 5-parameter ECOM1 model with BDS-3 a priori box-wing model
Satellite antenna PCO/PCV	BDS-3: PCOs according to CSNO/TARC (Table 3); ignoring PCVs GPS: igs14_2045.atx (Rebischung et al. 2016)
Receiver antenna PCO/PCV	Corrections for GPS L1/L2 are used for BDS-3 B1I/B3I
Solid earth tides, pole tides, and ocean tides	IERS conventions 2010 (Petit and Luzum 2010); FES2004 (Lyard et al. 2006) for ocean tides
Relativity	IERS conventions 2010
Phase wind-up	Corrected (Wu et al. 1993)
Tropospheric delay	Zenith troposphere delay and gradient parameters are estimated as piecewise constant with 2-h and 24-h interval, respectively.
Receiver clocks	Epoch-wise estimated; Constant ISBs of BDS-3 w.r.t. GPS for each receiver
Satellite clocks	Epoch-wise estimated
Phase ambiguities	Float constant for each continuous arc; double-differenced ambiguities resolution for GPS and BDS-3 separately
Earth Rotation Parameters	Polar motions and their drifts (Xpole, DXpole, Ypole, DYpole) are estimated; UT1 is fixed and its rate DUT1 is estimated

## Attitude control models of BDS-3 satellites

Most GNSS satellites keep the navigation antenna pointing toward the earth center and the solar panels perpendicular to the sunlight, by doing continuous rotation about their geocenter-pointing axis (Bar-Sever 1996; Kouba 2008). In the IGS-specific spacecraft body frames (Montenbruck et al. 2015a), the nominal yaw-angle  $\psi_{\text{nom}}$  is given by:

$$\psi_{\text{nom}} = \text{atan2}(S_{oy}, S_{ox}) \quad (1)$$

$S_{ox}$  and  $S_{oy}$  are two components of the sun vector

$$S_o = (S_{ox}, S_{oy}, S_{oz}) = (\sin \mu \cos \beta, -\sin \beta, \cos \mu \cos \beta) \quad (2)$$

where  $\beta$  is the elevation of the sun above the orbital plane and  $\mu$  is the orbital angle between satellite and orbital midnight. When the sun is close to the orbital plane ( $\beta \approx 0$  deg) while the satellite approaches the orbital noon ( $\mu \approx 180$  deg) or midnight ( $\mu \approx 0$  deg), the nominal yaw rate may exceed the maximum satellite hardware rate. Specific attitude control is employed to solve this dilemma. The attitude control laws of GPS and GLONASS were described by Bar-Sever (1996), Kouba (2008) and Dilssner et al. (2010b), respectively, and

the Galileo attitude laws were published by the European GNSS Service Centre (EGSC 2017).

Most BDS-2 IGSO and MEO satellites use two attitude control modes of YS and ON, and the switches between YS and ON take place when the sun elevation angle is approximately  $\pm 4$  deg (Dai et al. 2015). Nevertheless, BDS-2 IGSO C017 and C019, which were manufactured by CAST, were found to use a continuous YS mode (Dilssner 2017). The attitude mode of C017 and C019 is also applied by BDS-3S/BDS-3 CAST IGSO and MEO satellites (Li et al. 2018b). In this study, the specific yaw control model established by Dilssner (2017) is used for CAST satellites.

As for BDS-3 satellites manufactured by SECM, the yaw-attitude cannot be accurately estimated since the horizontal PCO is only a few centimeters. According to Xia et al. (2018), the SECM attitude control model is given as: when the sun elevation  $\beta$  is within  $\pm 3$  deg, the sun vector component  $S_{oy}$  is substituted by an auxiliary one  $S_{my}$ :

$$S_{my} = \begin{cases} -\sin(3 \text{ deg}) & \text{for } \beta > 0 \\ -\sin(-3 \text{ deg}) & \text{for } \beta < 0 \end{cases} \quad (3)$$

and the updated yaw-angle  $\psi_{\text{mod}}$  is expressed as

$$\psi_{\text{mod}} = \text{atan}2(S_{\text{my}}, S_{\text{ox}}) \quad (4)$$

The yaw-attitude angles during orbital noon (left) and midnight (right) of BDS-3 CAST C201 and SECM satellites C203 for  $\beta$  angles close to zero are shown in Fig. 2. The slew rates of the attitude models are much smaller than the nominal ones when passing the orbital noon and midnight. It is worth noting that for SECM satellites there is always a bias between the modeled and the nominal yaw-angles when the sun elevation angle is within  $\pm 3$  deg.

During the periods of low  $\beta$  angles, the observation residuals will increase once the yaw-attitude is mismodeled (Dilssner et al. 2010b). As a result, we use the observation residuals of LC combinations to analyze the influence of BDS-3 yaw-attitude law on POD. The RMS values of LC observation residuals for BDS-3 satellites during noon-turn and midnight-turn maneuvers are shown in Fig. 3. The blue bars are for the nominal yaw-steering attitude, and the red bar is for the attitude models with rate limitations. The LC residual RMS value during noon- and night-turns ( $|\mu| < 10$  deg or  $|\mu - 180$  deg|  $< 10$  deg) is reduced from 1.87 cm to 1.74 cm for CAST satellites after applying the attitude model, with an improvement of 7.0%. For SECM satellites, an improvement of 2.5% from 1.83 to 1.79 cm is also found in the LC residual RMS values. When compared to CAST satellites, the improvement of SECM satellites is less obvious, which can be due to the fact that the SECM PCOs in  $x$ - and  $y$ -axis are only 4 cm and 1 cm, respectively. Compared to CAST satellites with  $-20$  cm offset in the  $x$ -axis, the error of satellite antenna PCO corrections arisen from mismodeling yaw-attitude is much smaller for SECM satellites. As a result, the LC residual improvement caused by proper yaw-attitude modeling is less obvious for SECM satellites.

**Fig. 2** Modeled yaw-attitude angles during orbital noon (left) and midnight (right) of CAST (top) and SECM (bottom) satellites. Blue rhombuses represent nominal yaw-attitude angles, and the magenta squares represent modeled yaw-attitude angles

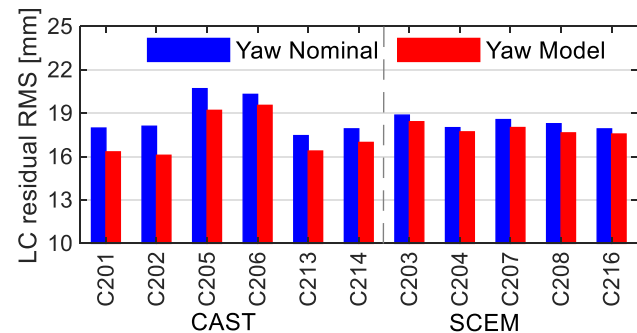
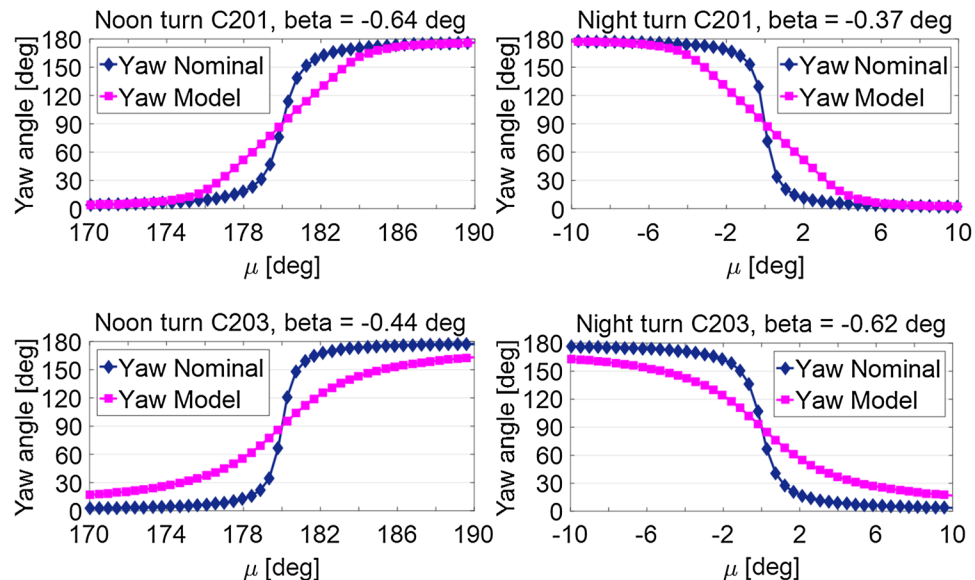


**Fig. 3** RMS values of LC residuals for BDS-3 satellites during noon-turn and midnight-turn maneuvers. Time periods are DOY 055–057 2019 for CAST satellites C201/C202/C205/C206/C213/C214, DOY 123–125 2019 for SECM satellites C207/C208/C216, and DOY 125–127 2019 for SECM satellites C203/C204, during which the  $\beta$  angles are within  $\pm 2$  deg

The 24-h orbit overlapping RMS values before and after applying the proper attitude models are shown in Fig. 4 in the along-track, cross-track, and radial components. Only the periods of  $|\beta| < 3$  deg are considered for the overlapping statistics. The blue bars are POD results of the nominal yaw-steering attitude, and the red bars are POD results of the attitude models with rate limitations. Satellites C209–C212 are not shown since during DOY 001–130 of 2019 the  $\beta$  angles of these four satellites are always higher than 3 deg. The overlapping RMS values of POD results with nominal attitude are (10.9, 4.5, 3.5) cm for CAST satellites and (13.2, 6.6, 4.4) cm for SECM satellites in the along-track, cross-track, and radial component, respectively. When the rate-limited attitude models are applied, the overlapping RMS can be reduced to (10.3, 4.0, 3.1) cm for CAST satellites and (12.7, 6.2, 4.1) cm for

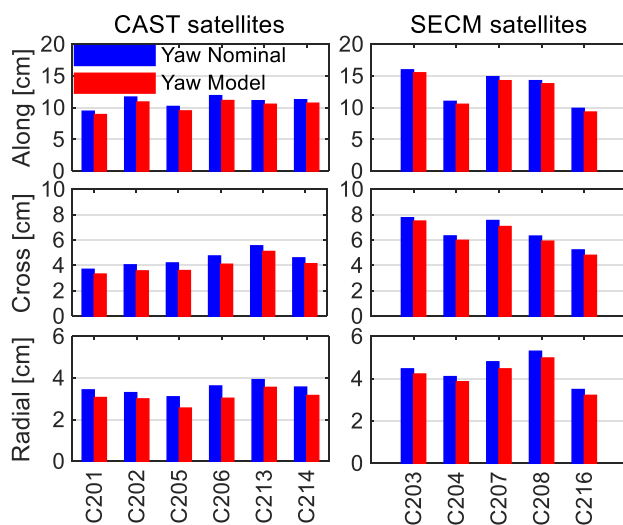


**Fig. 4** BDS-3 orbit overlapping RMS using a different attitude. Blue bars are for the POD results applying the nominal yaw-steering attitude, while the red bars are for those applying the attitude models with rate limitations

SECM satellites, with improvements of (5.5, 11.1, 11.4) % and (3.8, 6.1, 6.8) %.

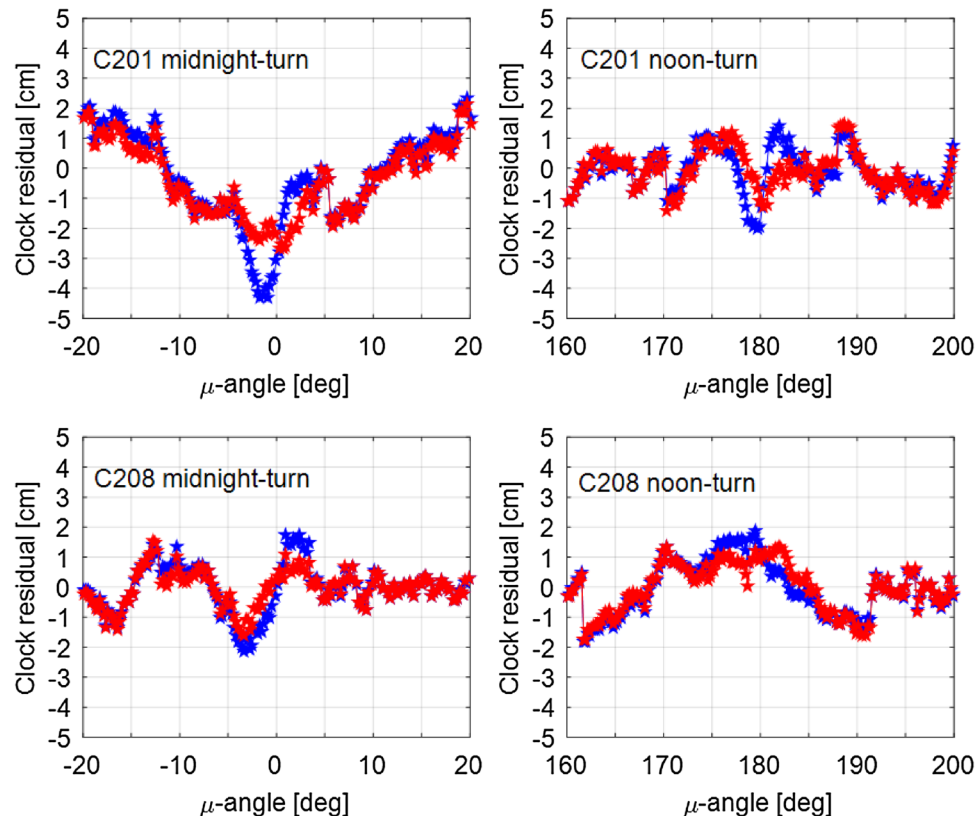
The satellite clock estimates are also affected by the mismodeling of yaw-attitude. As a result, we also evaluated the influences of yaw-attitude models on satellite clock

estimates. Figure 5 shows the clock residuals after the removal of the linear trend for CAST satellite C201 (top) and SECM satellite C208 (bottom) during midnight-turns (left) and noon-turns (right). As can be seen, large jumps can be found in the clock residuals around orbital midnight and noon if the nominal yaw-attitude is used (blue). However, when the rate-limited attitude models are applied (red), the clock residuals become smoother and more continuous, which provides another evidence for the benefits of proper attitude modeling.

### BDS-3 a priori box-wing SRP model

One defect of the purely empirical ECOM1 model is that the SRP perturbation is not fully absorbed, especially for satellites with non-cubic shapes. Adding higher-order periodic parameters to empirical models can better absorb the SRP perturbation. However, the higher-order periodic terms deteriorate the estimation of global geodetic parameters such as geocentric coordinates (Bury et al. 2019). On the other hand, the analytical box-wing model can account for most part of the SRP perturbation. By using the box-wing model as the a priori one and estimating a small number of empirical parameters, better POD performance can be achieved. The a priori box-wing model has been introduced for non-cubic-shaped satellites such as Galileo and QZSS (Montenbruck

**Fig. 5** Clock residuals with the nominal yaw-attitude (blue) and with rate-limited attitude models (red) for CAST satellite C201 (top) and SECM satellite C208 (bottom) during midnight-turns (left) and noon-turns (right)



et al. 2015b, 2017a; Steigenberger and Montenbruck 2016; Li et al. 2019; Bury et al. 2019).

In this section, we intend to establish an a priori SRP model for BDS-3 satellites. BDS-3 MEO satellites are based on two different satellite platforms developed by CAST and SECM. As reported by Xia et al. (2018), the SECM satellites have a body size of about  $X \times Y \times Z = 2.55 \text{ m} \times 1.01 \text{ m} \times 1.23 \text{ m}$  with an elongated shape along the  $X$ -axis (Xia et al. 2018), which is similar to Galileo satellites (EGSC 2017). Please note that the  $Z$ -axis is parallel to the navigation antenna direction and  $+Z$ -axis points toward the earth; the  $Y$ -axis is parallel to the rotation axis of the solar panels, and the  $+X$ -axis completes a right-handed system and points toward the hemisphere containing the sun (Montenbruck et al. 2015a). The surface area of a single-side solar array amounts to about  $5.4 \text{ m}^2$  for SECM BDS-3 MEO satellites. It should be noted that the solar panel size of  $4.7 \text{ m} \times 1.5 \text{ m}$  presented in Xia et al. (2018) includes the triangular brackets, which connect the solar panels to the satellite body. In this study, the triangular brackets are not considered, and the size of about  $3.6 \text{ m} \times 1.5 \text{ m}$  is used for SECM satellite's single-side solar array. For CAST satellites, the size of  $X \times Y \times Z = 1.66 \text{ m} \times 1.31 \text{ m} \times 2.18 \text{ m}$  and the surface area of about  $10.20 \text{ m}^2$  (CSNO 2019b) are used for satellite body and one-side solar array, respectively.

BDS-3 satellites adopt triple-junction gallium arsenide solar cells, which can greatly enhance the satellite energy absorption efficiency. This kind of solar cell has an absorption coefficient of about 0.92. For the satellite body, CAST satellites employ a kind of multilayer with an absorption coefficient of 0.36 and a specular reflection coefficient of 0. In addition, the  $-X$ ,  $+Y$ , and  $-Y$  surfaces of CAST satellites are covered by optical solar reflectors (OSRs). The OSR has an absorption coefficient of 0.135 and a specular reflection coefficient of 0.865. According to CSNO (2019b), the  $+X$  and  $-Z$  surfaces of CAST satellites are only covered by multilayers. As for the  $+Z$  surface of CAST satellites, it is reported to have an absorption coefficient of 0.92 (CSNO 2019b). Unfortunately, the specular reflection coefficient and the diffuse reflection coefficient of  $+Z$  surface are not

published. In this study, we assume that the specular reflection coefficient is 0.08 and the diffuse reflection coefficient is 0. As for SECM satellites, it is reported that all the six surfaces have the same absorption coefficient of 0.20 (CSNO 2019b). The specular reflection coefficient and the diffuse reflection coefficient of SECM satellite surfaces are assumed to be 0.80 and 0, since they are not published in CSNO (2019b). Please note that the navigation antenna on the  $+Z$  panel is not considered due to the lack of further knowledge about its area. The geometrical and optical properties used for CAST and SECM satellites are summarized in Table 5.

With the approximate geometrical and optical information, the BDS-3 box-wing model can be formulated and used as the a priori one. According to Fliegel et al. (1992), the radiation pressure acceleration of the satellite bodies can be expressed as

$$a = -\frac{A_i S_0}{M c} \cos \theta_i \left[ (\alpha_i + \delta_i) \left( \vec{e}_D + \frac{2}{3} \vec{e}_{N,i} \right) + 2\rho_i \cos \theta_i \vec{e}_{N,i} \right] \quad (5)$$

while the acceleration of the solar panels can be expressed as

$$a = -\frac{A_{SP} S_0}{M c} \cos \theta_{SP} \left[ (\alpha_{SP} + \delta_{SP}) \vec{e}_D + 2 \left( \frac{\delta_{SP}}{3} + \rho_{SP} \cos \theta_{SP} \right) \vec{e}_{N,SP} \right] \quad (6)$$

where the subscripts  $i$  and  $SP$  indicate the individual satellite body surface and solar panel surface, respectively.  $A$  is the surface area, and  $M$  is the mass of satellite.  $S_0$  is the solar flux at 1 AU, and  $c$  is the velocity of light.  $\alpha$ ,  $\rho$ , and  $\delta$  are the absorption, specular reflection, and diffuse reflection coefficients of each surface.  $\vec{e}_D$  is the satellite-sun unit vector, and  $\vec{e}_N$  is the unit vector normal to the body or solar panel surfaces.  $\vec{e}_D$  and  $\vec{e}_N$  enclose the angle  $\theta = \arccos(\vec{e}_D^T \vec{e}_N)$ . Please note that (6) is adopted for the solar panels under the assumption of a mostly balanced thermal re-emission from the front- and back-side of the panel (Montenbruck et al. 2017a).

In combination with the box-wing model, five ECOM1 parameters are estimated to absorb the unmolded SRP acceleration. A constant is estimated for each direction of the

**Table 5** Geometrical and optical properties of BDS-3 satellites

	Satellites	Mass/kg	Box-wing	Area/m <sup>2</sup>	Absorption	Specular reflection	Diffuse reflection
CAST BDS-3	941–1007		Wing	10.22*2	0.92	0.08	0.00
			+Z	2.18	0.92	0.08	0.00
			-Z	2.18	0.36	0.00	0.64
			+X	2.86	0.36	0.00	0.64
SECM BDS-3	1008–1045		Wing	5.40*2	0.92	0.08	0.00
			+Z	2.59	0.20	0.80	0.00
			-Z	2.59	0.20	0.80	0.00
			+X	1.25	0.20	0.80	0.00

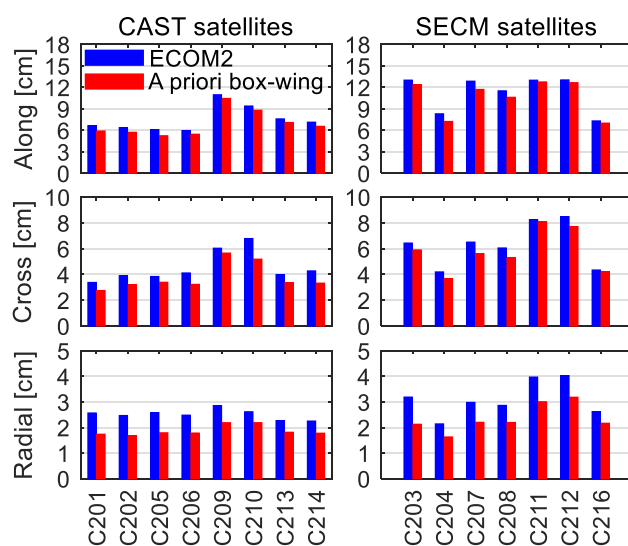


**Fig. 6** BDS-3 orbit overlapping RMS using different SRP models of ECOM2 and the BDS-3 a priori box-wing model

**Table 6** Offsets of LRA's effective phase center with respect to center of mass (CoM) for BDS-3 satellites (unit: mm)

SVN	Manufacturer	PCOX	PCOY	PCOZ
C202	CAST	594.7	84.6	1264.4
C206	CAST	598.6	-86.6	1265.0
C207	SECM	609.5	426.0	614.2
C208	SECM	609.7	427.3	615.3

**Fig. 7** One-way SLR residuals of BDS-3 CAST and SECM satellites with respect to the satellite-sun elongation angle. Left subfigures are the SLR residuals using ECOM2 SRP model, and right subfigures are those using the a priori box-wing model

right-handed DYB frame, and the first-order sine and cosine terms are only estimated for the B direction (Springer et al. 1999). Figure 6 illustrates the orbit overlapping RMS values of the a priori box-wing SRP model in comparison with the purely empirical ECOM2 model. ECOM2 model exhibits overlapping RMS values of (7.5, 4.5, 2.5) cm for CAST satellites and (11.3, 6.3, 3.1) cm for SECM satellites. When the BDS-3 a priori box-wing model is applied, the overlapping RMS values can be reduced to (6.9, 3.8, 1.9) cm for CAST satellites and (10.6, 5.8, 2.4) cm for SECM satellites.

## SLR validation

All BDS-3 satellites are equipped with laser retro-reflector arrays (LRA), and some of them, i.e., C202, C206, C207, and C208, have been tracked by the International Laser Ranging Service (ILRS; Pearlman et al. 2002) since August 2018. The offsets of LRA's effective phase center are listed in Table 6 for these four BDS-3 satellites (CSNO 2019b). Site coordinates, velocities, and eccentricities (ILRS 2018, 2019) based on the International Terrestrial Reference Frame ITRF2014 (Altamimi et al. 2016) are used for the SLR stations. Solid earth tides, polar tides, and ocean tidal loading corrections are applied to the SLR stations. The Mendes and Pavlis (2004) model is used to correct the atmospheric refraction. SLR measurements with range residuals exceeding values of 50 cm were excluded from the residual analysis. Figure 7 shows the one-way SLR residuals

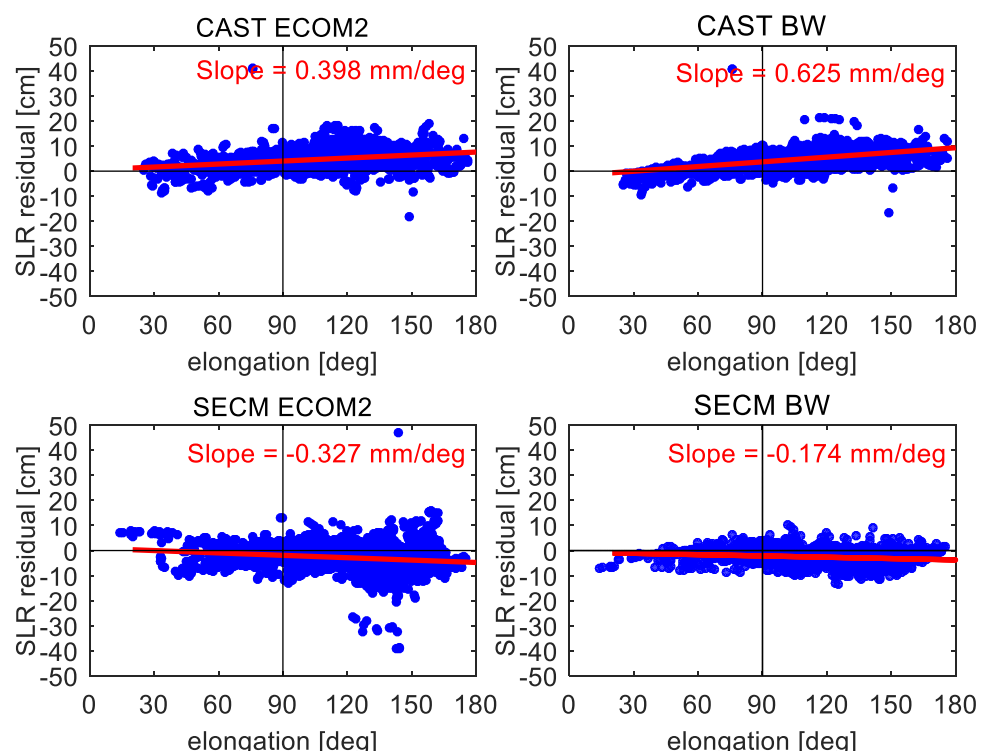


**Table 7** SLR validation of BDS-3 satellites with different SRP models (unit: cm)

SVN	ECOM2		A priori box-wing	
	Mean bias	STD	Mean bias	STD
CAST C202	3.6	3.4	3.1	3.1
CAST C206	4.9	4.3	4.6	4.2
SECM C207	-2.5	5.2	-2.3	3.5
SECM C208	-3.3	5.7	-3.0	3.7

of POD results using ECOM2 and the BDS-3 a priori box-wing SRP model as a function of the satellite-sun elongation angle. Most SLR residuals are within  $\pm 20$  cm. When ECOM2 SRP model is applied, the slopes are 0.40 mm/deg and -0.33 mm/deg for CAST and SECM satellites, respectively. When the a priori box-wing SRP model is applied, the residual dependency on the elongation angle can be reduced for SECM satellites, with the slope being -0.17 mm/deg. Nevertheless, the slope of CAST satellites is 0.63 mm/deg, which is larger than that of ECOM2. This indicates that current the a priori box-wing model has deficiencies in properly accounting the elongation-varied SRP accelerations of CAST satellites. In addition, the a priori box-wing model shows a notable curvature in the variation of residuals with elongation, which might be attributed to the simplification of a box-wing model and the neglect of the shading effects. The unmodeled accelerations caused by the albedo as well as the thermal radiation might also explain the notable curvature in SLR residuals.

Table 7 summarizes the statistics of SLR residuals for different SRP models. It is obvious that the a priori box-wing model has smaller standard deviation (STD) values when compared to ECOM2 model. In addition, the a priori box-wing model also presents slightly smaller mean biases. The smaller STD values as well as the smaller mean biases indicate that the geometrical and optical coefficients in Table 5 can be used for BDS-3 POD processing. Further improvements of the a priori box-wing model are expected when detailed information about the specular reflection coefficients and the diffuse reflection coefficients is officially released.

## Conclusions

We present the results of precise orbit determination for BDS-3 MEO satellites using iGMAS and MGEX networks. Several improvements in orbit modeling such as yaw-attitude control models and BDS-3 a priori box-wing model are demonstrated. Orbit overlapping comparison and SLR validation are applied to evaluate the POD results.

BDS-3 satellites apply continuous YS modes with rate-limitation. After modeling the yaw-attitude during deep eclipse seasons, the orbit overlapping can be improved by (0.6, 0.5, 0.4) cm for CAST satellites and by (0.5, 0.4, 0.3) cm for SECM satellites in the along-track, cross-track, and radial components, respectively. Proper attitude models also reduce the LC residual RMS of CAST and SECM satellites from 1.87 and 1.83 cm to 1.74 and 1.79 cm during deep eclipse seasons. In addition, the rate-limited attitude models can make the clock residuals smoother and more continuous during midnight-turns and noon-turns. With approximate satellite dimensions and optical properties, the BDS-3 a priori box-wing model is introduced and evaluated. Orbit overlapping RMS values of the BDS-3 a priori box-wing model are (6.9, 3.8, 1.9) cm for CAST satellites and (10.6, 5.8, 2.4) cm for SECM satellites, presenting improvements of (0.6, 0.7, 0.6) cm and (0.7, 0.5, 0.7) cm compared to ECOM2 model. The SLR residuals of the BDS-3 a priori box-wing model have mean biases of about 0–5 cm and STD values smaller than 5 cm. Compared to the ECOM2 model, the a priori box-wing model exhibits smaller SLR mean biases and STD values for CAST and SECM satellites.

**Acknowledgements** We would like to express our gratitude to iGMAS, IGS/MGEX and ILRS for providing GNSS and SLR observation data. This study is financially supported by the National Natural Science Foundation of China (Grant No. 41774030), the Hubei Province Natural Science Foundation of China (Grant No. 2018CFA081) and the National Youth Thousand Talents Program.

## References

- Altamimi Z, Rebischung P, Métivier L, Collilieux X (2016) ITRF2014: a new release of the International Terrestrial Reference Frame modeling nonlinear station motions. *J Geophys Res Solid Earth* 121(8):6109–6131. <https://doi.org/10.1002/2016jb013098>
- Arnold D, Meindl M, Beutler G, Dach R, Schaer S, Lutz S, Prange L, Sósnica K, Mervart L, Jäggi A (2015) CODE's new solar radiation pressure model for GNSS orbit determination. *J Geod* 89(8):775–791. <https://doi.org/10.1007/s00190-015-0814-4>
- Bar-Sever Y (1996) A new model for GPS yaw attitude. *J Geod* 70(11):714–723. <https://doi.org/10.1007/bf00867149>
- Bury G, Zajdel R, Sońska K (2019) Accounting for perturbing forces acting on Galileo using a box-wing model. *GPS Solut* 23(3):74. <https://doi.org/10.1007/s10291-019-0860-0>
- CSNO (2017a) BeiDou navigation satellite system signal in space interface control document—open service signal B1C (version 1.0). China Satellite Navigation Office, December 2017
- CSNO (2017b) BeiDou navigation satellite system signal in space interface control document—open service signal B2a (version 1.0). China Satellite Navigation Office, December 2017
- CSNO (2019a) Satellite antenna phase center of BDS. China Satellite Navigation Office, <http://en.beidou.gov.cn/SYSTEMS/Officialdocument/201912/P020200103555670269778.atx>
- CSNO (2019b) Satellite information of BDS. China Satellite Navigation Office, <http://en.beidou.gov.cn/SYSTEMS/Officialdocument/201912/P020200103556125703019.rar>

- Dai X, Ge M, Lou Y, Shi C, Wickert J, Schuh H (2015) Estimating the yaw-attitude of BDS IGSO and MEO satellites. *J Geod* 89(10):1005–1018. <https://doi.org/10.1007/s00190-015-0829-x>
- Dilssner F (2010) GPS IIF-1 satellite, antenna phase center and attitude modeling. *Inside GNSS* 5(6):59–64
- Dilssner F (2017) A note on the yaw attitude modeling of BeiDou IGSO-6, a report dated November 20, 2017. [http://navigation-ofce.esa.int/attachments\\_24576369\\_1\\_BeiDou\\_IGSO-6\\_Yaw\\_Modeling.pdf](http://navigation-ofce.esa.int/attachments_24576369_1_BeiDou_IGSO-6_Yaw_Modeling.pdf)
- Dilssner F, Springer T, Gienger G, Dow J (2010) The GLONASS-M satellite yaw-attitude model. *Adv Space Res* 47(1):160–171. <https://doi.org/10.1016/j.asr.2010.09.007>
- EGSC (2017) Galileo satellite metadata. European GNSS Service Centre. <https://www.gsc-europa.eu/support-to-developers/galileo-satellite-metadata>
- Fliegel H, Gallini T, Swift E (1992) Global positioning system radiation force model for geodetic applications. *J Geophys Res* 97(B1):559–568. <https://doi.org/10.1029/91jb02564>
- He L, Ge M, Wang J, Wickert J, Schuh H (2013) Experimental study on the precise orbit determination of the BeiDou navigation satellite system. *Sensors* 13(3):2911–2928. <https://doi.org/10.3390/s130302911>
- ILRS (2018) SLRF2014 station coordinates and velocities. International laser ranging service. [ftp://cddis.gsfc.nasa.gov/pub/slrf/products/resource/SLRF2014\\_POS+VEL\\_2030.0\\_180504.snx](ftp://cddis.gsfc.nasa.gov/pub/slrf/products/resource/SLRF2014_POS+VEL_2030.0_180504.snx)
- ILRS (2019) ILRS station eccentricities. International laser ranging service. [ftp://cddis.gsfc.nasa.gov/pub/reports/slrocc/ecc\\_une.snx](ftp://cddis.gsfc.nasa.gov/pub/reports/slrocc/ecc_une.snx)
- Jiao W, Ding Q, Li J, Lu X, Feng L, Ma J, Chen G (2011) Monitoring and assessment of GNSS open services. *J Navig* 64(S1):S19–S29. <https://doi.org/10.1017/s0373463311000385>
- Johnston G, Riddell A, Hausler G (2017) The international GNSS Service. In: Teunissen PJG, Montenbruck O (eds) Springer handbook of global navigation satellite systems. Springer International Publishing, Berlin, pp. 967–982. <https://doi.org/10.1007/978-3-319-42928-1>
- Kouba J (2008) A simplified yaw-attitude model for eclipsing GPS satellites. *GPS Solut* 13(1):1–12. <https://doi.org/10.1007/s1029-008-0092-1>
- Kouba J (2013) Noon turns for deep eclipsing Block IIF GPS satellites, a note prepared for IGS ACs, dated Dec 19, 2013 [IGS-ACS-930 Mail]
- Li X, Ge M, Dai X, Ren X, Fritsche M, Wickert J, Schuh H (2015) Accuracy and reliability of multi-GNSS real-time precise positioning: GPS, GLONASS, BeiDou, and Galileo. *J Geod* 89(6):607–635. <https://doi.org/10.1007/s00190-015-0802-8>
- Li X, Yuan Y, Zhu Y, Huang J, Wu J, Xiong Y, Zhang X, Li X (2018a) Precise orbit determination for BDS3 experimental satellites using iGMAS and MGEX tracking networks. *J Geod* 93(1):103–117. <https://doi.org/10.1007/s00190-018-1144-0>
- Li X, Hu X, Guo R, Tang C, Zhou S, Liu S, Chen J (2018b) Orbit and positioning accuracy for new generation BeiDou satellites during the Earth eclipsing period. *J Navig* 71(5):1069–1087. <https://doi.org/10.1017/s0373463318000103>
- Li X, Yuan Y, Huang J, Zhu Y, Wu J, Xiong Y, Li X, Zhang K (2019) Galileo and QZSS precise orbit and clock determination using new satellite metadata. *J Geod* 93(8):1123–1136. <https://doi.org/10.1007/s00190-019-01230-4>
- Lu M, Li W, Yao Z, Cui X (2019) Overview of BDS III new signals. *Navigation* 66(1):19–35. <https://doi.org/10.1002/navi.296>
- Lyard F, Lefevre F, Letellier T, Letellier T, Francis O (2006) Modelling the global ocean tides: modern insights from FES2004. *Ocean Dyn* 56(5–6):394–415. <https://doi.org/10.1007/s1023-006-0086-x>
- Mendes VB, Pavlis EC (2004) High-accuracy zenith delay prediction at optical wavelengths. *Geophys Res Lett*. <https://doi.org/10.1029/2004gl020308>
- Montenbruck O, Hauschild A, Steigenberger P (2014) Differential code bias estimation using multi-GNSS observations and global ionosphere maps. *Navigation* 61(3):191–201. <https://doi.org/10.1002/navi.64>
- Montenbruck O, Schmid R, Mercier F, Steigenberger P, Noll C, Fatkulin R, Kogure S, Ganeshan AS (2015a) GNSS satellite geometry and attitude models. *Adv Space Res* 56(6):1015–1029. <https://doi.org/10.1016/j.asr.2015.06.019>
- Montenbruck O, Steigenberger P, Hugentobler U (2015b) Enhanced solar radiation pressure modeling for Galileo satellites. *J Geod* 89(3):283–297. <https://doi.org/10.1007/s00190-014-0774-0>
- Montenbruck O, Steigenberger P, Darugna F (2017a) Semi-analytical solar radiation pressure modeling for QZS-1 orbit-normal and yaw-steering attitude. *Adv Space Res* 59(8):2088–2100. <https://doi.org/10.1016/j.asr.2017.01.036>
- Montenbruck O et al (2017b) The multi-GNSS experiment (MGEX) of the international GNSS service (IGS)—achievements, prospects and challenges. *Adv Space Res* 59(7):1671–1697. <https://doi.org/10.1016/j.asr.2017.01.011>
- Pavlis N, Holmes S, Kenyon S, Factor J (2012) The development and evaluation of the earth gravitational model 2008 (EGM2008). *J Geophys Res Solid Earth*. <https://doi.org/10.1029/2011jb008916>
- Pearlman M, Degnan J, Bosworth J (2002) The international laser ranging service. *Adv Space Res* 30(2):135–143. [https://doi.org/10.1016/s0273-1177\(02\)00277-6](https://doi.org/10.1016/s0273-1177(02)00277-6)
- Petit G, Luzum B (2010) IERS Conventions 2010. No.36 in IERS Technical Note, Verlag des Bundesamtes für Kartographie und Geodäsie, Frankfurt am Main
- Rebischung P, Schmid R, Herring T (2016) Upcoming switch to IGS14/igs14.atx. *IGSMAIL-7399*. <https://lists.igs.org/pipermail/igsmail/2016/001233.html>
- Rodriguez-Solano C, Hugentobler U, Steigenberger P (2012) Adjustable box-wing model for solar radiation pressure impacting GPS satellites. *Adv Space Res* 49(7):1113–1128. <https://doi.org/10.1016/j.asr.2012.01.016>
- Shi C, Zhao Q, Li M, Tang W, Hu Z, Lou Y, Zhang H, Niu X, Liu J (2012) Precise orbit determination of Beidou satellites with precise positioning. *Sci China Earth Sci* 55(7):1079–1086. <https://doi.org/10.1007/s11430-012-4446-8>
- Springer T, Beutler G, Rothacher M (1999) A new solar radiation pressure model for GPS satellites. *GPS Solut* 2(3):50–62. <https://doi.org/10.1007/pl00012757>
- Standish E (1998) JPL planetary and lunar ephemerides DE405/LE405. Interoffice Memorandum IOM 312.F-98-048, Jet Propulsion Laboratory, Pasadena
- Steigenberger P, Montenbruck O (2016) Galileo status: orbits, clocks, and positioning. *GPS Solut* 21(2):319–331. <https://doi.org/10.1007/s10291-016-0566-5>
- Steigenberger P, Hugentobler U, Hauschild A, Montenbruck O (2013) Orbit and clock analysis of compass GEO and IGSO satellites. *J Geod* 87(6):515–525. <https://doi.org/10.1007/s00190-013-0625-4>
- Tan B, Yuan Y, Wen M, Ning Y, Liu X (2016) Initial results of the precise orbit determination for the new-generation BeiDou satellites (BeiDou-3) based on the iGMAS network. *ISPRS Int J Geo Inf* 5(11):196. <https://doi.org/10.3390/ijgi5110196>
- Villiger A (2019) IGS14\_2056: Update including Beidou-3S and Beidou-3 satellites. *IGSMAIL-7782*. <https://lists.igs.org/pipermail/igsmail/2019/007778.html>
- Wang C, Guo J, Zhao Q, Liu J (2018) Solar radiation pressure models for BeiDou-3 I2-S satellite: comparison and augmentation. *Remote Sens* 10(1):118. <https://doi.org/10.3390/rs10010118>
- Wanninger L, Beer S (2015) BeiDou satellite-induced code pseudorange variations: diagnosis and therapy. *GPS Solut* 19(4):639–648. <https://doi.org/10.1007/s10291-014-0423-3>
- Wu J, Wu S, Hajj G, Bertiger W, Lichten S (1993) Effects on antenna orientation on GPS carrier phase. *Manuscr Geod* 18(2):91–98

- Xia L, Lin B, Liu Y, Xiong S, Bai T (2018) Satellite geometry and attitude mode of MEO satellites of BDS-3 developed by SECM. In: Proceedings of the ION GNSS 2018, Institute of Navigation, Miami, Florida, USA, September 24–28, pp 1268–1289. <https://doi.org/10.33012/2018.16118>
- Xiao W, Liu W, Sun G (2016) Modernization milestone: BeiDou M2-S initial signal analysis. *GPS Solut* 20(1):125–133. <https://doi.org/10.1007/s10291-015-0496-7>
- Xu X, Wang X, Liu J, Zhao Q (2019) Characteristics of BD3 global service satellites: POD, open service signal and atomic clock performance. *Remote Sens* 11(13):1559. <https://doi.org/10.3390/rs11131559>
- Yan X, Huang G, Zhang Q, Liu C, Wang L, Qin Z (2018) Early analysis of precise orbit and clock offset determination for the satellites of the global BeiDou-3 system. *Adv Space Res* 63(3):1270–1279. <https://doi.org/10.1016/j.asr.2018.10.038>
- Yan X, Liu C, Huang G, Zhang Q, Wang L, Qin Z, Xie S (2019) A priori solar radiation pressure model for BeiDou-3 MEO satellites. *Remote Sens* 11(13):1605. <https://doi.org/10.3390/rs1131605>
- Yang Y, Li J, Xu J, Tang J, Guo H, He H (2011) Contribution of the COMPASS satellite navigation system to global PNT users. *China Sci Bull* 56(26):2813–2819. <https://doi.org/10.1007/s11434-011-4627-4>
- Yang Y, Tang J, Montenbruck O (2017) Chinese navigation satellite systems. In: Teunissen PJG, Montenbruck O (eds) Springer handbook of global navigation satellite systems. Springer International Publishing, Berlin, pp 273–304. [https://doi.org/10.1007/978-3-319-42928-1\\_10](https://doi.org/10.1007/978-3-319-42928-1_10)
- Zhang X, Li X, Lu C, Wu M, Pan L (2017a) A comprehensive analysis of satellite-induced code bias for BDS-3 satellites and signals. *Adv Space Res* 63(9):2822–2835. <https://doi.org/10.1016/j.asr.2017.11.031>
- Zhang X, Wu M, Liu W, Li X, Yu S, Lu C, Wickert J (2017b) Initial assessment of the COMPASS/BeiDou-3: new-generation navigation signals. *J Geod* 91(10):1225–1240. <https://doi.org/10.1007/s00190-017-1020-3>
- Zhang B, Jia X, Sun F, Xiao K, Dai H (2019) Performance of BeiDou-3 satellites: signal quality analysis and precise orbit determination. *Adv Space Res* 64(3):687–695. <https://doi.org/10.1016/j.asr.2019.05.016>
- Zhao Q, Wang C, Guo J, Wang B, Liu J (2017) Precise orbit and clock determination for BeiDou-3 experimental satellites with yaw attitude analysis. *GPS Solut* 22(1):4. <https://doi.org/10.1007/s10291-017-0673-y>

**Publisher's Note** Springer Nature remains neutral with regard to jurisdictional claims in published maps and institutional affiliations.



**Xingxing Li** is currently a professor at Wuhan University. He has completed his B.Sc. degree at the School of Geodesy and Geomatics at Wuhan University. He obtained his Ph.D. degree at the Department of Geodesy and Remote Sensing of the German Research Centre for Geosciences (GFZ). His current research mainly involves GNSS precise data processing and its application for geosciences.



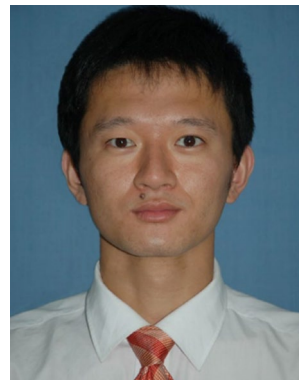
**Yongqiang Yuan** is currently a Ph.D. candidate at Wuhan University. He has completed his B.Sc. and Master's degree at the School of Geodesy and Geomatics at Wuhan University in 2016 and 2019. His area of research currently focuses on GNSS precise orbit determination.



**Yiting Zhu** is currently a Master candidate at Wuhan University. She has completed her B.Sc. at the School of Geodesy and Geomatics at Wuhan University in 2018. Her area of research currently focuses on multi-GNSS precise orbit determination.



**Wenhui Jiao** is currently a professor at the Beijing Institute of Tracking and Telecommunication Technology. He received his Ph.D. degree in 2003 from Shanghai Astronomical Observatory, Chinese Academy of Sciences. His research work is focused on GNSS navigation.



**Lang Bian** is currently a senior engineer at the China Academy of Space Technology (Xi'an). He received his Master's degree from the China Academy of space technology (Xi'an) in 2010. He has been researching on satellite navigation augmentation technology, especially satellite autonomous integrity monitoring (SAIM) and the payload onboard.



**Xin Li** is currently a Ph.D. candidate at Wuhan University. She has completed her B.Sc. at the School of Geodesy and Geomatics at Wuhan University in 2015. Her area of research currently focuses on multi-GNSS PPP ambiguity resolution.



**Keke Zhang** is currently a Ph.D. candidate at Wuhan University. He has completed his B.Sc. at the School of Geodesy and Geomatics in Wuhan University in 2016. His area of research currently focuses on precise orbit determination for LEO satellites.